

Approximate Entropy Analysis for Nonlinear Beam Dynamics

Yongjun Li ^{1,*}

¹*Brookhaven National Laboratory, Upton 11973, New York, USA*

In this paper, we apply approximate entropy (ApEn) analysis to the nonlinear beam dynamics in circular accelerators. Due to the presence of strong nonlinear magnets, chaos of beam motion gradually increases with amplitude. Such chaos can be quantitatively characterized with ApEn of beam turn-by-turn readings. Then ApEn, as a chaos indicator, can be used for nonlinear lattice optimization and analysis.

I. INTRODUCTION

For circular particle accelerators, the nonlinearities of beam dynamics confine long-term motions to be stable only within a limited region in 6-dimensional phase space, namely, dynamic aperture (DA) [1]. Even within DA, particle motions could still be chaotic. It is commonly believed that, for a given magnetic lattice, through suppressing chaos, one can enlarge its DA and local momentum acceptance (LMA), and also enhance its robustness to errors. Therefore, various chaos indicators have been adopted to characterize the nonlinearities of beam motions [2], such as the Lyapunov exponent (LE) [3–5], frequency map analysis (FMA) [6], forward-reversal integration (FRI) [7–9], data-driven chaos indicator [10], fluctuation of approximate invariant [11], etc. In this paper we apply approximate entropy (ApEn) to analyze the nonlinear beam dynamics.

The concept of entropy has its origins in classical physics under the second law of thermodynamics. In the context of nonlinear dynamics, information entropy is central in quantifying the degree of uncertainty or information gain, and is therefore widely used to explain complex nonlinear behavior in real-world systems. Among many entropy analyses, ApEn conception was initially developed by Pincus [12] to analyze medical data, such as heart rate, and later spread its applications in many other fields, such as finance [13], and nonlinear dynamics [14], etc. It is a technique used to quantify the amount of regularity and the unpredictability of fluctuations particular for short and noise time-series data.

Due to the presence of strong nonlinear magnetic fields in circular accelerators, the chaos of beam motions gradually increase with amplitude. Such chaos is often visualized with the Poincaré map, i.e., the intersection of a periodic orbit projected in a certain lower-dimensional subspace, usually a 2-dimensional coordinate-momentum phase space. Experimentally it can also be observed from turn-by-turn (TBT) data after beam is excited. ApEn can quantitatively characterize the chaos of circulating beam TBT readings. Based on that, we can determine if magnetic lattices are well configured or not. Thus, ApEn, as a chaos indicator, can be used for nonlinear lat-

tice optimization at design stage, or online beam-based optimization as well [15] if BPMs have TBT resolution.

The remainder of this paper is outlined as follows: Sect. II reviews the definition of ApEn and explains its principle briefly. Then ApEn analysis is applied to a Hénon map as a proof-of-principle in Sect. III. In Sect. IV, ApEn observed in the transverse x - y plane are used as minimization objectives to optimize the National Synchrotron Light Source II (NSLS-II) nonlinear lattice. In Sect. V, we implement a detailed ApEn analysis for an elite candidates selected from the previous optimization, and interpret physics information being conveyed by such analysis. A summary is given in Sect. VI.

II. APPROXIMATE ENTROPY

According to Pincus [12], ApEn is defined as: Two input parameters, m and r , must be fixed to compute ApEn, m is the “length” of compared runs, and r is effectively a filter. Given N data point $u = u(1), u(2), \dots, u(N)$ form vector sequences $x(1)$ through $x(N - m + 1)$, with $m \leq N$ define by $x(i) = u(i), u(i + 1), \dots, u(i + m - 1)$. These vectors represent m consecutive u values, starting with the i^{th} point. Define the distance $d[x(i), x(j)]$ between $x(i)$ and $x(j)$ as the maximum difference in their respective scalar components, $d[x(i), x(j)] = \max_{k=1,2,\dots,m} (|u(i + k - 1) - u(j + k - 1)|)$. Then we calculate the value $C_i^m(r) = (\text{number of } j \leq N - m + 1 \text{ such that } d[x(i), x(j)] \leq r) / (N - m + 1)$. The numerator of C_i^m counts, within the tolerance r , the number of blocks of consecutive values of length m which are similar to the pattern of window length m . Then the C_i^m 's measure the regularity, or frequency, of patterns similar to this window. Define

$$\varphi^m(r) = \frac{1}{N - m + 1} \sum_{i=1}^{N-m+1} \log C_i^m(r), \quad (1)$$

where \log is the natural logarithm. The ApEn is defined as

$$\text{ApEn}(m, r, N)(u) = \lim_{N \rightarrow \infty} \varphi^m(r) - \varphi^{m+1}(r), \quad (2)$$

which is a measure of system complexity. Fundamentally, ApEn measures the conditional probability that nearby pattern runs remain close in the next incremental comparison. A positive ApEn usually indicates a chaos [16]

* email: yli@bnl.gov

. The value of N , the number of input data points for ApEn computations, is typically between 75 and 5,000. Based on the calculations that included both theoretical analysis and clinical applications, Pincus concluded that, for $m = 1, 2$, values of filter r between 0.1 to 0.25 standard deviation of the $u(i)$ data can produce good statistical validity [17]. We found that such settings are also applicable to nonlinear beam dynamics for circular accelerators.

ApEn can be computed directly based on the above definition. It requires execution time analogous to the square of the size of the input signal. Fast algorithms, such as [18], were proposed to speed up its computation. In the meantime, well-developed and documented computation packages, such as EntropuHub [19] (used in this paper), are also available.

III. APPLICATION TO HÉNON MAP

In this section, ApEn analysis is applied to a 1-dimensional Hénon's quadratic area-preserving map [20],

$$\begin{pmatrix} x \\ p \end{pmatrix}_n = \begin{pmatrix} \cos \mu & \sin \mu \\ -\sin \mu & \cos \mu \end{pmatrix} \begin{pmatrix} x \\ p - \lambda x^2 \end{pmatrix}_{n-1}. \quad (3)$$

From the view of beam dynamics, this discrete map represents a thin-lens sextupole kick followed by a linear phase space rotation at a phase advance $\mu = 2\pi\nu$. Here, sextupole strength $\lambda = 1$, and the linear tune is chosen to be $\nu = 0.205$ to observe the 5th-order resonance at certain amplitudes. The map is iterated for 512 runs, then the ApEn's of x -coordinates are computed for each initial condition in the phase space x - p as illustrated in Fig. 1. Its ApEn (chaos) increase gradually with the initial condition's amplitude $\sqrt{x^2 + p^2}$, except while crossing stable resonances. The contours of FMA and FRI analyses are also computed for the purpose of comparison.

Note that, while crossing stable resonances, the behavior of FMA differs from ApEn and FRI analyses. Fig. 2 shows four trajectories in the Poincaré section x - p , while a 5th order resonance is being crossed driven by the amplitude dependent detuning. When the tune is sufficiently close to 0.2, and some trajectories are trapped by elliptic fixed points, five isolated islands are formed and then gradually merge to five fixed points. Around those stable fixed points, the fundamental tune diffusions are relatively large (at the order of $10^{-5\sim 6}$). However, the dimension of islands is relatively small, then time-series data composed of x (or p) is highly regular with a low periodicity, which yields near zero ApEn. Similar behaviors are observed in the difference of FRIs as well [8]. It could be explained as, for an on-resonance but stable time-series data, its regularity is higher in the time domain than in the frequency domain. Another observation from Fig. 1 is that, the FMA and ApEn could provide more rich information (having more fine structures in their chaos maps) than the FRI analysis. It means they could be more sensitive to the variations of chaos.

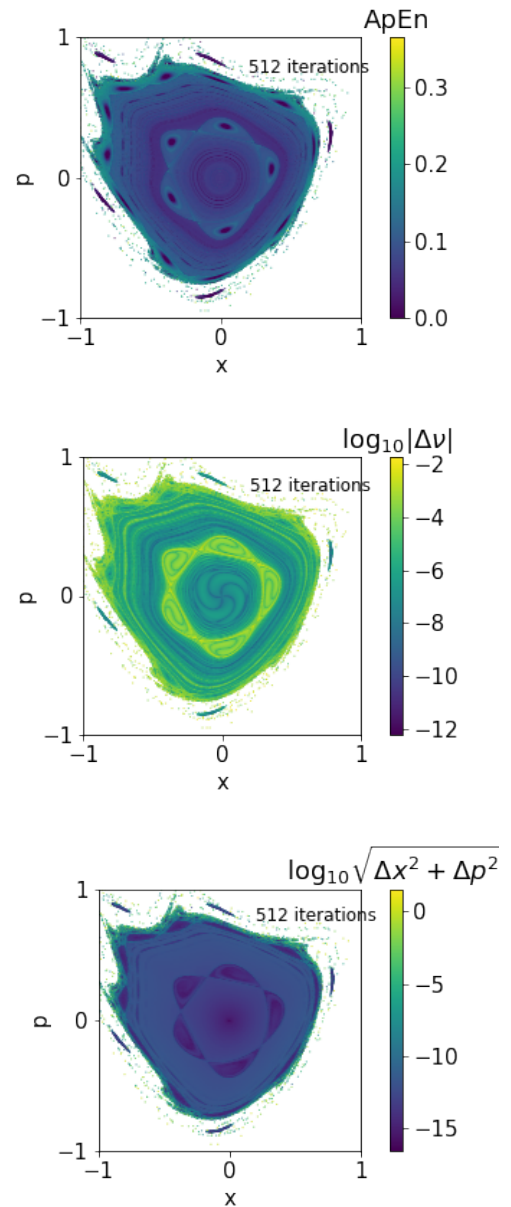


Figure 1. (Colored) Comparison of the ApEn (top), FMA (middle) and FRI (bottom) analyses for a Hénon map with 512 iterative runs. The color-maps represent the ApEn, tune diffusion and distance between forward and reversal trajectories respectively at the locations of their initial conditions. The blank area represents unbounded trajectories.

IV. APPLICATION TO NONLINEAR LATTICE OPTIMIZATION

In this section, we use ApEn as chaos indicator to optimize the nonlinear lattice for the NSLS-II storage ring. In a linearly stable lattice, the motion of particle, seen by a BPM at a certain location, is a periodical time-series oscillating with a fixed frequency, known as the linear tune. Nonlinear magnets, such as sextupoles for chro-

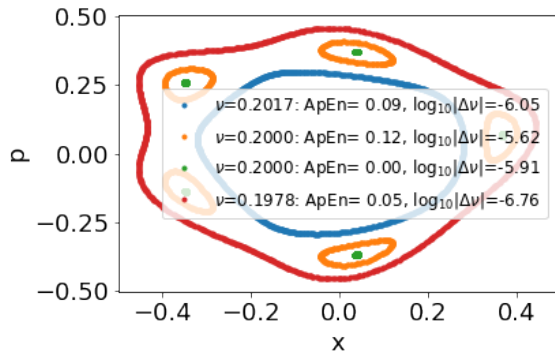


Figure 2. (Colored) Trajectories of the Hénon map in the x - p phase space while crossing the 5th order resonance stably. Once tune is sufficiently close to 0.2, and trajectories are trapped by elliptic fixed points, motions in the time domain become highly regular with a low periodicity 5, then near-zero ApEns are observed.

maticity correction, can perturb regular motions. Thus, signals seen by the BPM now have fluctuations on top of regular motions. The ApEn of TBT BPM readings reflects the likelihood that similar patterns of the TBT readings will not be followed by additional similar readings. Given a nonlinear lattice, if the ApEns of TBT readings are low, the beam motion is less chaotic, and vice versa. By minimizing the ApEn of different trajectories through tuning nonlinear knobs, the lattice could be optimized. Usually, ApEn analysis can let chaos be visible from a short time-series with only several tens of data. It means that, only short-term TBT data is needed to drive optimizer. At the early stage of lattice design, such low computation cost can efficiently narrow down the search range by ruling out bad candidates.

Next, we explain the detailed optimization implementations using the NSLS-II storage ring as an example. From a certain longitudinal observation location (the injection point in this example), multiple initial conditions are uniformly populated within a Region of Interest (RoI) with a transverse dimension $x \in [-40, 40]$ $y \in [0, 15]$ mm (Fig. 3). The RoI should be chosen slightly larger than the desired dynamic aperture. Particle trajectories are simulated with a symplectic integrator [21] implemented in the code ELEGANT [9]. Each trajectory is simulated for $N = 256$ turns if survived, and TBT data at the observation point is recorded, then used to compute its ApEn.

The goal of optimization is minimizing the ApEns for all initial conditions within the RoI. It is neither practical nor necessary to minimize every initial condition simultaneously, therefore, the RoI is divided into several zones as shown in Fig. 3. For each zone, two objectives are the horizontal and vertical ApEns averaged over all initial conditions if survived after $N = 256$ turns. By tuning the sextupole knobs, we attempt to minimize each zone's ApEns simultaneously to suppress the overall chaos in-

side the whole RoI. The reason of choosing $N = 256$ turns is that such data-sets are already long enough to measure the chaos with ApEn. In the meantime, the computation cost needed for particle tracking simulation is relatively low. Usually, most light source rings are composed of multiple identical cells, therefore, we can even use one cell to optimize the DA for the ideal error-free lattice to narrow down the search range quickly. Then in the next stage, a full ring lattice including various imperfections is used to search robust solutions within a narrow range.

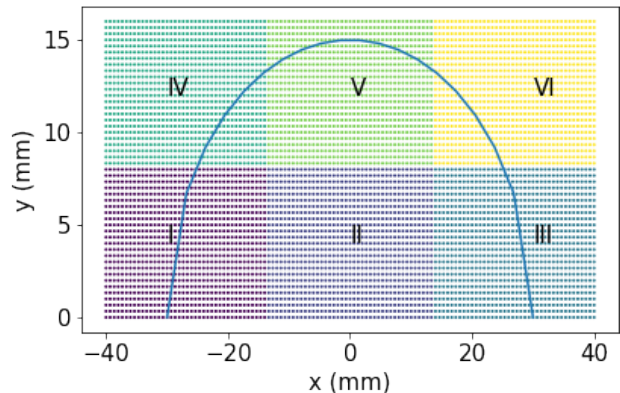


Figure 3. (Colored) Dividing the region of interest (RoI) into $2 \times 3 = 6$ zones in the x - y plane at the observation. In each zone, multiple initial conditions (represented with same-colored dots) are uniformly populated. The optimization objectives are the averaged ApEns of all initial conditions within each individual zone. The solid line is the desired DA profile for the NSLS-II storage ring.

ApEn need be computed in the horizontal and vertical planes respectively, and they are usually at different scales and need to be minimized separately. Then the number of optimization objectives is two times the number of zones. The tuning knobs in this example are the normalized gradients K_2 of six harmonic sextupole families. The range of K_2 is within $[-40, 40]$ (m^{-3}) limited by their power supply capacities and magnetic saturation. These harmonic sextupoles doesn't contribute to the linear chromaticity, but can compensate the geometric and chromatic optics abbreviations generated by chromaticity correction sextupoles.

This multi-objective optimization is solved with the widely used genetic algorithm [22–24]. A small population with 1,000 candidates evolves more than 30 generations, a good convergence of the average ApEn has been reached (Fig. 4). The DAs of all candidates in the 30th generation are calculated for picking up some elite candidates among them. The on-momentum DA profiles of top 20 elites are illustrated in the top subplot of Fig. 5. It is interesting to observe that the distributions of their six knobs (sextupole gradients K_2) also converge to some small ranges as shown in the bottom subplot. The corre-

lation between the average ApEns and the area of DAs is illustrated in Fig. 6, which confirms that suppressing the ApEns in both the horizontal and vertical planes is essential in enlarging DA.

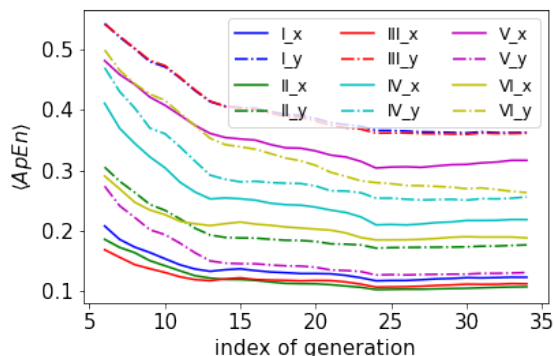


Figure 4. (Colored) Convergence of averaged ApEns in the genetic algorithm optimization. Solid lines stand for the horizontal plane, and dashed-dotted ones for the vertical plane. Lines with a same color are from the same zone.

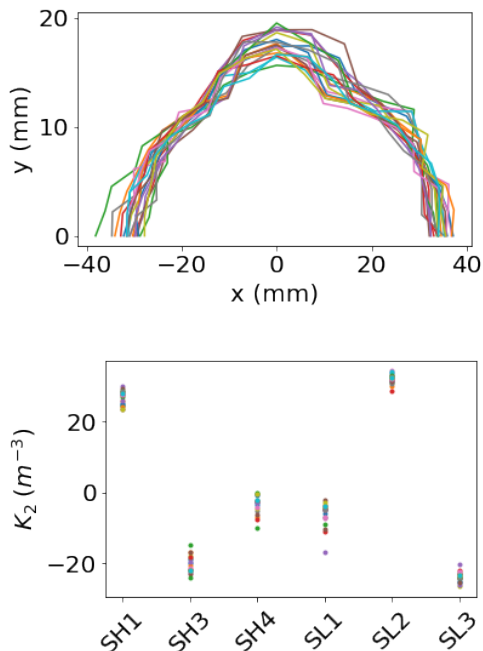


Figure 5. (Colored) Top: on-momentum DA profiles for 20 elites selected from the last generation of the genetic optimization. Bottom: distribution of six sextupole knob configurations of these elites. They converge to some narrow ranges as well.

In designing a nonlinear lattice, the DA and local momentum acceptance (LMA) must be considered simultaneously to satisfy the requirements on the injection efficiency and beam lifetime [25]. A same strategy as

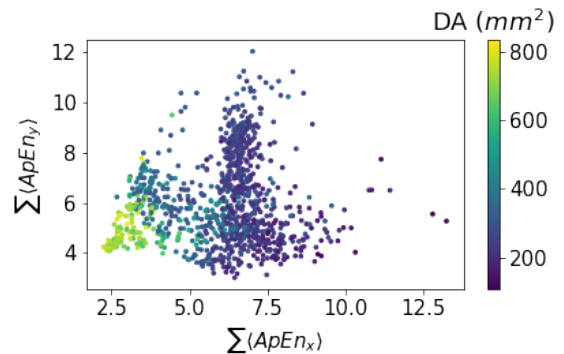


Figure 6. (Colored) Correlation between ApEn and DA. The horizontal and vertical axes are the sums of six zone's averaged ApEns. Each dot represents one candidates in the 30th generation of the genetic optimization, colored with its area of on-momentum DA. The correlation confirms that having small ApEns in both the horizontal and vertical planes is essential to enlarge the NLSL-II ring DA.

ref. [8] is used to include some off-momentum DAs as optimization objectives. In this example, on $\delta = \pm 2.5\%$ off-momentum planes, ApEns are added as the objectives, which are evaluated in the same way as Fig. 3. Considering off-momentum DAs could be smaller than the on-momentum one, slightly tight ROIs can be used. The on- and two off-momentum ($\delta = \pm 2.5\%$) DAs for a selected elite candidate are illustrated in Fig. 7, which should be sufficient to achieve high-efficient injections and 3 hours Touschek beam lifetime [26] by comparing with our current operation lattice.

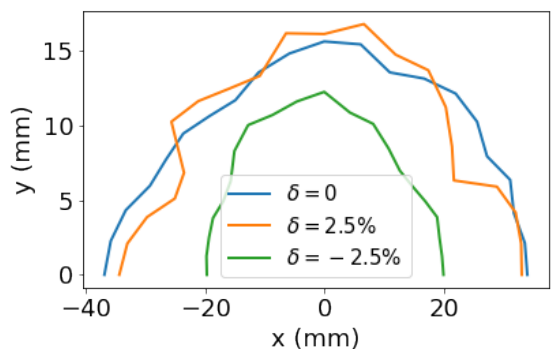


Figure 7. (Colored) On- and two off-momentum DAs for a selected elite candidate.

V. INFORMATION LEARNED FROM APEN

Like FMA or FRI etc., ApEn can also provide detailed chaos information for a given nonlinear lattice, such as the strength and location of resonances, and robustness

to errors. Below we use one of elite candidates (the same one as shown in Fig. 7) as an example to implement a detailed ApEn analysis. To achieve a more accurate result, for each initial condition, a $N = 1024$ long TBT data is obtained with the code ELEGANT. In the meantime, high density initial conditions are populated to produce a high-resolution DA profile to identify resonance lines. As already observed in Fig. 4, the horizontal and vertical ApEns are at different scales. Therefore, three ApEn profiles are provided in Fig. 8: two separated ApEn maps observed in either the horizontal or vertical plane solely, and one weighted map obtained by adding them after normalizing with their maxima,

$$\text{ApEn}_{x,y} = \frac{\text{ApEn}_x}{\max \text{ApEn}_x} + \frac{\text{ApEn}_y}{\max \text{ApEn}_y}, \quad (4)$$

where $\max \text{ApEn}_{x,y}$ are the maxima in each planes respectively.

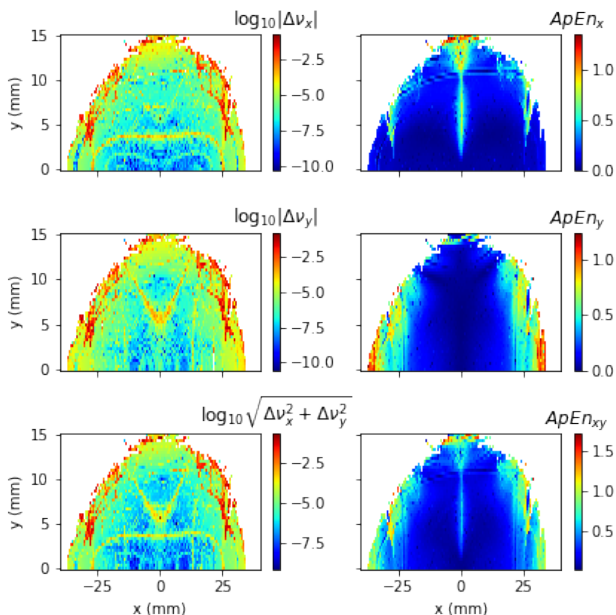


Figure 8. (Colored) FMA and ApEn analyses for a selected elite candidate. Left column: Tune diffusion maps of FMA observed in the horizontal, vertical and both planes; Right column: ApEn maps observed in the horizontal, vertical and both planes.

In the horizontal ApEn_x map, besides visible resonances around $x = \pm 20 \text{ mm}$, strong chaos also appears in the vicinity of y -axis ($x = 0$), particularly when $y \geq 10 \text{ mm}$. While in the vertical plane, strong chaos shows up when $x \geq |20| \text{ mm}$. Based on this observation, we can conclude that, a strong nonlinear cross-talking must exist between two transverse planes. Such cross-talking drives the vertical motion to be chaotic at large horizontal amplitudes and vice versa. In the vicinity of y -axis, small amplitude horizontal TBT data is polluted by the coupling from the vertical plane, thus its signal-noise-ratio is low, which only cause some visual chaos

there. The real problem is that, such cross-talking would cause horizontal DA to reduce significantly in the presence of vertical physical apertures and errors. We use the ApEn_y (see Fig. 8’s middle-right subplot) to further illustrate this consequence. When particle’s horizontal amplitude exceeds 20 mm , although the horizontal motions remain regular (shown with “cold” colors in the top-right subplot), their vertical motions become chaotic dramatically and should have large fluctuations while observing their TBT data. Particles can still survive in an open space. However, once small vertical physical apertures and errors are in place, they can be scraped. Such cross-talking has a practical effect for every light source rings, in which in-vacuum undulators (IVU) usually have a few millimeters vertical apertures, and cause a significant reduction of DA in the horizontal plane. Note that most of light source rings need a sufficient horizontal DA for injection. As shown in Fig. 9, after a $\pm 2.5 \text{ mm}$ vertical aperture is imposed and the existing NSLS-II magnet systematic multipole errors are included, the horizontal DA immediately reduces to the area with low ApEn_y . If only the area of DA in free space is used as the objective of optimization, some candidates might be estimated optimistically. Previously, such difficulty has been overcome by including physical apertures and errors into the tracking simulation and optimization [25], but it greatly slows down the speed of optimization. One of the benefits of using ApEn as the chaos indicator is that, even with error-free magnet models, the robustness of lattice to errors and physical apertures could be visible and under consideration to a certain extent. Therefore, ApEn could be particularly useful in the early stage of lattice optimization to narrow down the search range for robust solutions, even with lack of information on magnet errors.

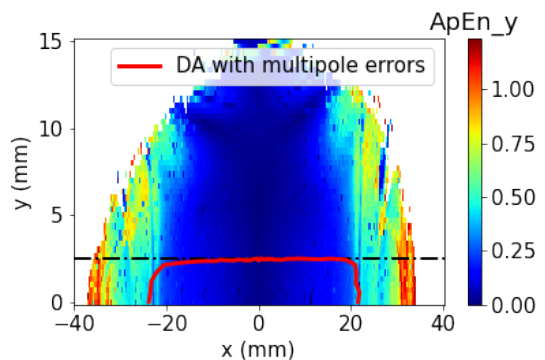


Figure 9. (Colored) Reduction of DA when a vertical physical aperture (dash-dot line) and multipole errors are imposed. The horizontal aperture is lost in the area where the vertical ApEn is high. The survived DA (red solid line) confirms that having low ApEn is essential to obtain robust solutions.

The standard FMA analyses are also illustrated in the left column of Fig. 8 for comparison. Three tune diffusion maps (in the horizontal, vertical and both planes respectively) gradually increase with their initial ampli-

tude, but there is no obvious jump between the regular and chaotic regime as shown in the subplot of $ApEn_y$ profile. However, FMA does provide a much clear view on resonances.

VI. SUMMARY

We introduce the ApEn concept to analyze the chaos of nonlinear beam dynamics. Using the TBT data observed by BPMs, nonlinear lattice configurations can be optimized through suppressing their ApEn. Two advantages of using ApEn are its low computational demand and robustness to noise [12]. ApEn can be designed to work for small data samples. It might be particularly useful in online beam-based optimization for electron storage rings. Because, valid TBT data can last only a few hundreds, or even a few tens turns due to strong radiation damping and beam decoherence. another advantage is, when data is noisy, the ApEn measure can be compared to the noise level in the data to determine what quality of true information may be present in the data. These advantages might make ApEn be a suitable objective for not only lattice design but also online optimization.

In the meantime, some limitations also exist in the ApEn analysis [27]. The algorithm counts each sequence as matching itself to avoid the occurrence of $\log(0)$ in the calculations. This step might introduce bias in ApEn, which causes ApEn to have two poor properties in prac-

tice: ApEn is heavily dependent on the record length and is uniformly lower than expected for short records. The ApEn analysis sometimes lacks relative consistency. That is, if ApEn of one data set is lower than that of another, it should, but does not, remain lower for all conditions tested. Particularly, in the vicinity of low order resonances, although TBT readings are regular due to a low periodicity, such motions are vulnerable to errors. Therefore, it might be better to use ApEn along with other chaos maps, such as FMA and FRI, to identify the chaos from different aspects in the nonlinear beam dynamics. All these chaos maps share same times-series (TBT data) and can be implemented in parallel.

Beside ApEn, many other entropy algorithms, such as Kolmogorov-Sinai entropy [28, 29], sample entropy [27], Fuzzy entropy [30], etc., are also available for analyzing nonlinear systems. Each algorithm has its pros and cons in quantifying chaos. Some further exploration on applying entropy analysis to beam dynamics might be interesting and fruitful.

ACKNOWLEDGMENTS

This research used resources of the National Synchrotron Light Source II, a U.S. Department of Energy (DOE) Office of Science User Facility operated for the DOE Office of Science by Brookhaven National Laboratory under Contract No. DE-SC0012704.

-
- [1] A. Chao, M. Tigner, H. Weise, and F. Zimmermann, *Handbook of accelerator physics and engineering*, 3rd ed. (World Scientific, 2023) Chap. 2.3.7, p. 140.
 - [2] A. Bazzani, M. Giovannozzi, C. E. Montanari, and G. Turchetti, “Performance analysis of indicators of chaos for nonlinear dynamical systems,” *Phys. Rev. E* **107**, 064209 (2023).
 - [3] A. Wolf, J. Swift, H. Swinney, and J. Vastano, “Determining lyapunov exponents from a time series,” *Physica D: nonlinear phenomena* **16**, 285–317 (1985).
 - [4] F. Schmidt, F. Zimmermann, and F. Willeke, “Comparison of methods to determine long-term stability in proton storage rings,” *Part. Accel.* **35**, 249–256 (1991).
 - [5] S. Habib and R. Ryne, “Symplectic calculation of lyapunov exponents,” *Phys. Rev. Lett.* **74**, 70–73 (1995).
 - [6] J. Laskar, “Introduction to frequency map analysis,” *Hamiltonian systems with three or more degrees of freedom*, 134–150 (1999).
 - [7] F. Panichi, K. Goździewski, and G. Turchetti, “The reversibility error method (REM): a new, dynamical fast indicator for planetary dynamics,” *Monthly Notices of the Royal Astronomical Society* **468**, 469–491 (2017).
 - [8] Y. Li, Y. Hao, K. Hwang, R. Rainer, A. He, and A. Liu, “Fast dynamic aperture optimization with forward-reversal integration,” *Nuclear Instruments and Methods in Physics Research Section A: Accelerators, Spectrometers, Detectors and Associated Equipment* **988**, 164936 (2021).
 - [9] M. Borland, *Elegant: A flexible SDDS-compliant code for accelerator simulation*, Tech. Rep. Advanced Photon Source LS-287 (Argonne National Lab., IL (US), 2000).
 - [10] Y. Li, J. Wan, A. Liu, Y. Jiao, and R. Rainer, “Data-driven chaos indicator for nonlinear dynamics and applications on ssftorage ring lattice design,” *Nuclear Instruments and Methods in Physics Research Section A: Accelerators, Spectrometers, Detectors and Associated Equipment* **1024**, 166060 (2022).
 - [11] Y. Li, K. Hwang, C. Mitchell, R. Rainer, R. Ryne, and V. Smaluk, “Design of double-bend and multibend achromat lattices with large dynamic aperture and approximate invariants,” *Physical Review Accelerators and Beams* **24**, 124001 (2021).
 - [12] S. Pincus, “Approximate entropy as a measure of system complexity.” *Proceedings of the National Academy of Sciences* **88**, 2297–2301 (1991).
 - [13] S. Pincus and R. Kalman, “Irregularity, volatility, risk, and financial market time series,” *Proceedings of the National Academy of Sciences* **101**, 13709–13714 (2004).
 - [14] C. Volos, S. Jafari, J. Munoz-Pacheco, J. Kengne, and K. Rajagopal, “Nonlinear dynamics and entropy of complex systems with hidden and self-excited attractors II,” (2020).
 - [15] X. Huang, “Robust simplex algorithm for online optimization,” *Physical Review Accelerators and Beams* **21**, 104601 (2018).
 - [16] J. Eckmann and D. Ruelle, “Ergodic theory of chaos and

- strange attractors,” *Reviews of modern physics* **57**, 617 (1985).
- [17] S. Pincus, “Approximate entropy (apen) as a complexity measure,” *Chaos: An Interdisciplinary Journal of Nonlinear Science* **5**, 110–117 (1995).
- [18] G. Manis, “Fast computation of approximate entropy,” *Computer methods and programs in biomedicine* **91**, 48–54 (2008).
- [19] M. Flood and B. Grimm, “Entropyhub: An open-source toolkit for entropic time series analysis,” *PloS one* **16**, e0259448 (2021).
- [20] M. Hénon, “Numerical study of quadratic area-preserving mappings,” *Quarterly of applied mathematics* , 291–312 (1969).
- [21] H. Yoshida, “Construction of higher order symplectic integrators,” *Phys. Lett.* **A150**, 262–268 (1990).
- [22] K. Deb, A. Pratap, S. Agarwal, and T. Meyarivan, “A fast and elitist multiobjective genetic algorithm: Nsga-ii,” *IEEE transactions on evolutionary computation* **6**, 182–197 (2002).
- [23] L. Yang, Y. Li, W. Guo, and S. Krinsky, “Multiobjective optimization of dynamic aperture,” *Phys. Rev. ST Accel. Beams* **14**, 054001 (2011).
- [24] Y. Li, W. Cheng, L-H. Yu, and R. Rainer, “Genetic algorithm enhanced by machine learning in dynamic aperture optimization,” *Phys. Rev. Accel. Beams* **21**, 054601 (2018).
- [25] M. Borland, L. Emery, V. Sajaev, and A. Xiao, “Multi-objective Optimization of a Lattice for Potential Upgrade of the Advanced Photon Source,” *Conf.Proc.* **C110328**, 2354–2356 (2011).
- [26] C. Bernardini, G. Corazza, G. Di Giugno, G. Ghigo, J. Haissinski, P. Marin, R. Querczoli, and B. Touschek, “Lifetime and beam size in a storage ring,” *Physical Review Letters* **10**, 407 (1963).
- [27] J. Richman and J. Moorman, “Physiological time-series analysis using approximate entropy and sample entropy,” *American journal of physiology-heart and circulatory physiology* (2000).
- [28] A. Shiriyayev, “New metric invariant of transitive dynamical systems and automorphisms of lebesgue spaces,” *Selected Works of AN Kolmogorov: Volume III: Information Theory and the Theory of Algorithms* , 57–61 (1993).
- [29] Y. Sinai, “Kolmogorov-sinai entropy,” *Scholarpedia* **4**, 2034 (2009).
- [30] A. De Luca and S. Termini, “A definition of a nonprobabilistic entropy in the setting of fuzzy sets theory,” in *Readings in Fuzzy Sets for Intelligent Systems* (Elsevier, 1993) pp. 197–202.